

# Revealing Nanostructures in High-Entropy Alloys via Machine-Learning Accelerated Scalable Monte Carlo Simulation

Xianglin Liu<sup>†\*</sup>

*Pengcheng Laboratory, Shenzhen, China*

Kai Yang<sup>†</sup>

*Pengcheng Laboratory, Shenzhen, China*

Yongxiang Liu

*Pengcheng Laboratory, Shenzhen, China*

Fanli Zhou

*School of Computer and Artificial Intelligence, Xiangnan University, Chenzhou, China*

Dengdong Fan

*Pengcheng Laboratory, Shenzhen, China*

Zongrui Pei

*New York University, NY 10012, USA*

Pengxiang Xu<sup>\*</sup>

*Pengcheng Laboratory, Shenzhen, China*

Yonghong Tian

*School of AI for Science, Shenzhen Graduate School, Peking University, Shenzhen, China*

*Pengcheng Laboratory, Shenzhen, China*

---

## Abstract

Large-scale simulations are a powerful tool for understanding material behavior and designing new materials. However, the computational limitations of atomistic-scale simulations—stemming from constraints in computational power, algorithmic efficiency, and accuracy—prevent us from modeling large systems, even at ground state, let alone at finite temperatures, with density functional theory (DFT)-level precision. Here, we introduce an efficient and **Scalable Monte Carlo (SMC)** method that overcomes the parallelization

---

*Email addresses:* xianglinliu01@gmail.com (Xianglin Liu<sup>†\*</sup>), xupx@pcl.ac.cn (Pengxiang Xu<sup>\*</sup>)

<sup>†</sup> These two authors contributed equally to this work

<sup>\*</sup> corresponding author

bottlenecks inherent in conventional MC simulation algorithms, reducing the computational complexity of an MC sweep from  $O(N^2)$  to  $O(N)$ . Leveraging the large degree of parallelization inherent in our method, we present a GPU-accelerated implementation, **SMC\_GPU**, which enables the simulation of atomistic systems exceeding **one billion atoms** while maintaining the accuracy of density functional theory (DFT). Using this unprecedented capability, we perform large-scale thermodynamic simulations to investigate the microstructure evolution in the FeCoNiAlTi and MoNbTaW high-entropy alloys (HEAs). Our results reveal a **rich diversity of nanoscale phenomena**, including short-range and long-range order, nanoparticles, and nanophases. The **size, composition, and morphology** of these nanostructures, which can comprise millions of atoms and thus present significant challenges for traditional methods, are analyzed with high-accuracy atomistic simulations for the first time, to the best of our knowledge. Our simulations produce thermodynamic properties and nanostructures that align well with available theoretical and experimental data. More intriguingly, our results reveal that the intricate nanoscale interplay of order and disorder in high-entropy alloys (HEAs) stems from the combined effects of chemical complexity and temperature, offering valuable guidance for alloy design. This work underscores the promising potential of large-scale MC simulation in exploring the largely uncharted territory of **nanoscale order-disorder evolution** in chemically complex materials.

*Keywords:* Monte Carlo Simulation, High Entropy Alloys, GPU Acceleration, Machine Learning, Nanostructures, Order-Disorder Transition

---

## 1. Introduction

A central goal of computational materials science is to predict the physical properties of materials using only fundamental inputs such as atomic species and physical constants. A widely adopted strategy towards this goal is the direct solution of the quantum equations governing electron dynamics: the Schrödinger equation for non-relativistic cases and the Dirac equation for relativistic cases. However, the complexity of quantum many-body interactions necessitates approximations. For such a purpose, density functional theory (DFT) [1] has emerged as a particularly successful approach, which approximates intractable many-body effects through an exchange-correlation functional within a single-body framework. This approximation significantly enhances computational efficiency, enabling the routine prediction of ground-state physical properties for systems with several hundred atoms. However, for systems requiring hundreds to thousands of atoms to simulate, such as nanodefects, non-stoichiometric compounds, and complex solid-solution alloys, conventional DFT becomes prohibitively expensive due to its intrinsic  $O(N^3)$  scaling with system size. A further com-

plication arises when considering finite-temperature effects [2]. Even for relatively small systems, rigorously accounting for temperature necessitates the evaluation of an enormous number of configurations, making DFT-based finite-temperature simulations computationally intractable. For example, a direct thermodynamic simulation of the CuZn alloy using a 250-atom supercell requires the calculation of 600,000 DFT energies [3], a task demanding some of the world’s largest supercomputers. Consequently, many compelling materials science problems remain beyond the reach of state-of-the-art (SOTA) first-principles methods.

One common strategy to accelerate atomistic simulations is to replace computationally expensive electronic structure calculations with computationally efficient atomistic models. From the perspective of renormalization group theory [4, 5], the atomistic models can be interpreted as the effective model obtained by integrating out the electronic degrees of freedom, which substantially reduces the computational cost. Indeed, traditional interatomic potentials, such as the embedded atom model (EAM), are widely employed for large-scale thermodynamic simulations. However, a critical limitation of these methods lies in their reliance on hand-crafted features and extensive trial-and-error tuning by domain experts, which restricts their generalization capability and predictive accuracy. On the other hand, the advent of machine learning (ML) for atomistic systems [6, 7, 8, 9] has introduced a new paradigm to the construction of effective atomistic models [10, 11, 12, 13, 14]. Instead of being predefined, the parameters in ML atomistic models are automatically determined by training from high-quality first-principles datasets, therefore rendering it possible for the model to automatically capture complex interatomic interactions [15, 16, 17, 18]. Well-trained ML models are typically orders of magnitude faster than DFT methods, while can still retain their high accuracy [19, 20, 21]. This renders it possible to carry out high-accuracy atomistic simulations using supercells containing millions of atoms [22, 23, 24, 25], far exceeding the thousands-of-atoms limits of conventional DFT approaches.

However, most machine learning potentials have been developed primarily to accelerate molecular dynamics (MD) simulations [22, 23, 7, 26, 27], with relatively limited applications in Monte Carlo (MC) simulations [28, 29, 16, 30, 29]. This is notable given that MC represents one of the two cornerstone methods in atomistic simulations, alongside MD [31]. A key challenge lies in the intrinsic sequential updating nature of widely used MC algorithms, such as the Metropolis algorithm, where the MC trials are generally attempted site by site, which hinders large-scale parallelization. This is in stark contrast to MD, where all the atoms are updated simultaneously in a single step. The sequential updating nature of MC quickly becomes the bottleneck as the system size grows, which undermines the efficiency advantage of ML atomistic models when integrating the two. On the other hand, for many interesting phenomena [32, 33, 34], such as order-disorder transitions in chemically complex

materials, MC simulations remain the only viable approach due to their ability to efficiently sample the entire phase space. Consequently, developing highly scalable MC algorithms that overcome the limitations of sequential updating is of paramount importance for enabling the widespread integration of MC and ML atomistic models.

To overcome the parallelization bottleneck inherent in conventional MC simulations, we introduce the Scalable Monte Carlo (SMC) method, which is a generalized checkerboard algorithm [35] that reduces the computational complexity of an MC sweep from  $O(N^2)$  to  $O(N)$ . Compared to the checkerboard algorithm variant [35] that only applies to Ising interactions, we demonstrate that the SMC method can be generalized to non-Ising interactions via the introduction of a local-interaction-zone of interatomic interactions, which renders it suitable for integration with machine learning atomistic models. We employ our method to study high-entropy alloys (HEAs) [36, 37], a class of chemically complex materials that have received significant attention due to their exceptional mechanical properties. These properties include overcoming the traditional strength-conductivity trade-off [38, 39, 40], attributed to phenomena such as chemical short-range order [41, 42, 43], nanoprecipitates [39], and nanophases [44]. Understanding these features necessitates large-scale MC simulations. Beyond mechanical properties, the size and morphology of nanostructures in HEAs also offer promising opportunities for catalysis, sparking widespread interest in recent years [45, 46, 47]. We present a GPU-accelerated implementation of the SMC method and apply it to investigate the nanostructure evolution in the  $\text{Fe}_{29}\text{Co}_{29}\text{Ni}_{28}\text{Al}_7\text{Ti}_7$  and  $\text{MoNbTaW}$  HEAs, employing two simple machine learning energy models using the local short-range order parameters [48, 33, 49] as input features. We demonstrate the high efficiency of our method for large-scale MC simulation, which enables the simulation of atomistic systems exceeding one billion atoms using a single GPU (graphic processing unit). The large-scale simulation reveal a rich diversity of nanoscale phenomena, and we present a detailed analysis in the result section of this work.

## 2. Results

### 2.1. Performance of the SMC algorithm

Our algorithm can be seen as a generalization of the checkerboard algorithm for the 2D Ising model, as explained in Supplementary 5.1. The key insight lies in rendering sequential Monte Carlo (MC) trials independent by partitioning the system into sufficiently large link-cells, thereby isolating the influence of individual MC trial moves. To simplify the explanation, a schematic of the link-cell for the 2D square lattice is shown in Fig. 1 (a). Each site is labeled by two indices  $(i_C, i_A)$ , where  $i_C$  represent different link-cells and  $i_A$  represents

the different atoms within the link-cell. For the sake of discussion, let us assume that the atoms have only nearest-neighbor interactions. In such a case, the MC updates of the atoms with the same  $i_A$  index but different  $i_C$  index are independent of each other. This obviously presents a parallelism opportunity. For instance, consider atom (1, 13). During MC update, atom (1, 13) can swap with any of its nearest neighbors (1, 12), (1, 14), (1, 8) and (1, 18), which are colored as yellow in Fig. 1(a). Due to the short interaction range (nearest-neighbor), these moves would have no impact on calculating the energy changes for the swap moves of atom ( $i_C, 13$ ) (red sites in Fig. 1(a)), and the degree of parallelism is the number of cells  $n_C$ . We denote the yellow and green sites surrounding each red site in Fig. 1 as a local-interaction zone (LIZ), which is a name inspired by the locally self-consistent multiple scattering (LSMS) method [50, 51]. In other words, for any two sites, as long as the MC trial of one site does not affect the energies of the LIZ of the other site, then these two sites are independent. It is easy to see that the above discussion based on the 2D square lattice can be easily extended to the case of 3D crystal. Furthermore, a domain decomposition scheme is introduced in the SMC method to distribute the lattice across multiple GPUs, which further enhances the achievable system size, as illustrated in Fig. 1 (b). Generally, to determine the energy change resulting from the MC swap trial at site  $i$ , the local energies of each site within the local interaction zone (LIZ) of site  $i$  must be evaluated. Additionally, chemical environment information extending beyond the LIZ is required for the energy change calculation, as illustrated by the LIZ+ region in Fig. 1 (c). Note that for a pair-interaction model, the above discussion can be simplified since the total energy changes can be calculated from the local energies of the two sites involved in the swap trial. As a result, the speed of the effective pair-interaction (EPI) model is faster than the generalized nonlinear model by approximately a factor of 50, as shown in Fig. 1 (d).

To illustrate the strength of our method, we compare the speed of the SMC method with other possible schemes to integrate MC with high-accuracy energy prediction methods, such as DFT, linear-DFT, and GNN (graph neural networks), as shown in Fig. 1, in which the lines are drawn by extrapolating from a data point using ideal scaling behavior. The actual computational speeds of the various methods are inherently influenced by numerous factors, such as the hardware, software implementations, material systems, and computational parameters. Therefore, the discussion presented here is intended solely to provide a theoretical estimation of their relative performance in terms of orders of magnitude. The stars in the figure represents the measured values of the SMC method, and the lines show the ideal scaling behaviors. For DFT and linear-DFT, we assume that an 100-atoms SCF calculation takes one hour, based on our experience with the MuST-KKR code [52]. The speed of the GNN method (Allegro) is estimated from the  $\text{Li}_3\text{PO}_4$  structure of 421,824 atoms in Ref. [24]. Note

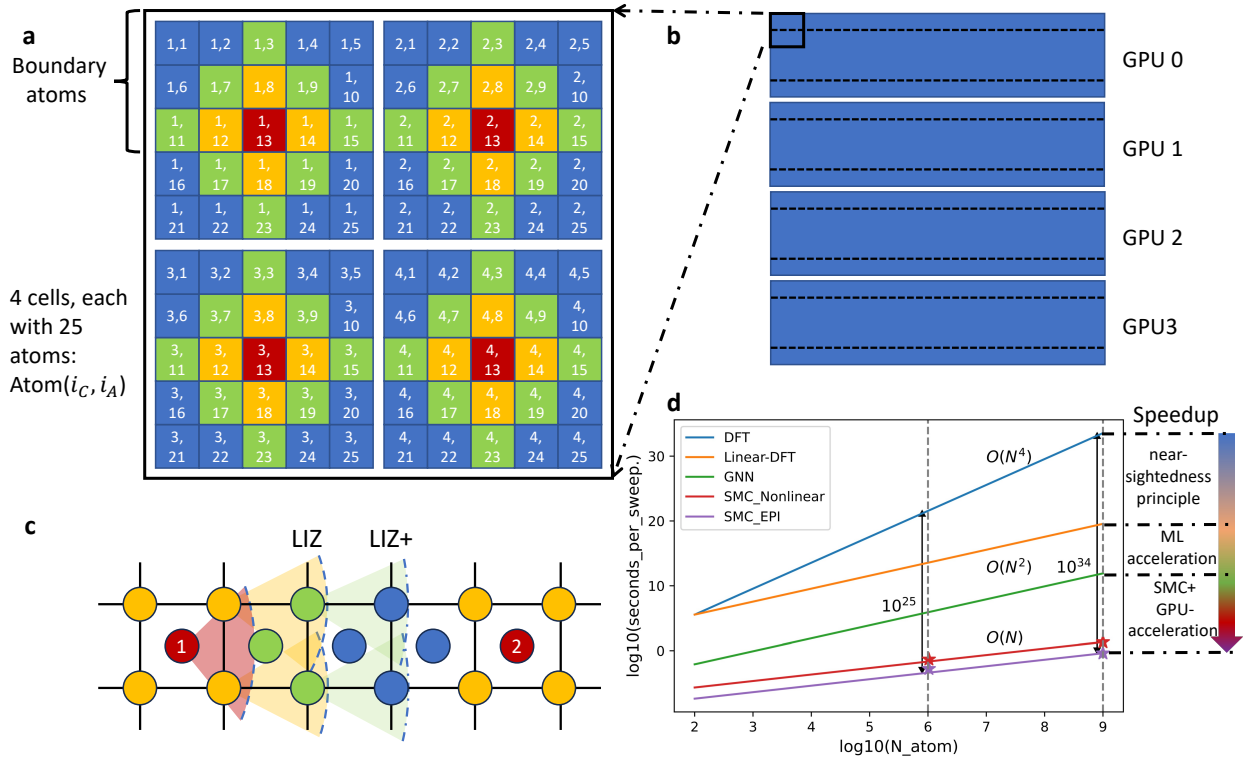


Figure 1: Schematics of the scalable Monte Carlo (SMC) method. (a) Illustrate the SMC method with a 2D square lattice, in which each site is denoted by two indices  $(i_C, i_A)$ , where  $i_C$  represents different link-cells, and  $i_A$  represents the different atoms within the  $n_A$  atom cell. (b) The whole chemical configuration is distributed on multiple GPUs, and the atoms near the boundary need to be communicated between GPUs  $n_A$  times in every MC sweep. (c) A 2D view of the fcc or bcc lattice, site 1 (red) can swap with each of its nearest neighboring sites (yellow), and the green sites represent the ones that the local energies can be affected. The yellow and green sites, together with the centering atom form the LIZ. The chemical environment with LIZ+ are needed to calculate the energy change due to a swap trial. (d) A log-log plot of computation time vs the system size to illustrate the speed-up ratio of the SMC method as compared to DFT (MuST-KKR), linear-DFT (LSMS), and GNN (Allegro). The measured values for SMC are signified as stars, and ideal scaling assumed for all lines.

that a MC sweep is defined as making a MC trial move over each lattice sites. Combining it with the intrinsic  $O(N^3)$  scaling in the DFT method, the total computational cost of DFT then scales as  $O(N^4)$ , as signified in Fig. 1 (d). Building on the principles of near-sightedness [53], the LSMS method employs an approximation that confines electron scattering to a local interaction zone. This approximation reduces the computational cost of energy evaluation to linear-scaling, therefor the total computational cost for a MC sweep scales approximately as  $O(N^2)$ . For a one million-atom system, the decreased computational complexity can reduce the cost by a factor of  $10^8$ , as shown in the orange line in Fig. 1 (d). Nevertheless, linear-DFT still requires solving the Schrödinger equations explicitly. By replacing the computationally expensive DFT method with machine learning models such as the GNN model, the computationally cost can be further reduced by a factor of  $10^8$ , as shown in the green line in Fig. 1

(d). Moreover, our SMC parallelization strategy significantly reduces the computational cost by replacing the energy evaluation of the whole system with calculating the energy changes of the LIZ, which is independent of the system size. This strategy further decrease the computational complexity to  $O(N)$ , which amounts to a speedup of  $10^6$  for a one million atom system. Finally, the SMC method can simultaneously harness the thousands or tens of thousands of cores in a modern high-performance GPU (e.g. 14,592 FP32 CUDA cores in an Nvidia H-800 GPU). For the EPI model, we estimate the GPU implementation contributes a speedup of  $10^3$ . Based on the preceding discussion, the total acceleration ratio of the SMC\_GPU method relative to a CPU based DFT method, for a system of  $N$  atoms, can be decomposed into contributions from nearsightedness  $S_{NS}$ , ML acceleration  $S_{ML}$ , SMC method  $S_{SMC}$ , and GPU acceleration  $S_{GPU}$ , and written as:

$$S = S_{NS} \times S_{ML} \times S_{SMC} \times S_{GPU} \approx (N/100)^2 \times 10^8 \times N \times 10^3 = 10^7 \times N^3, \quad (1)$$

as illustrated in Fig. 1 (d). Therefore, for a one million atom system, we have  $S = 10^{25}$ , as highlighted in Fig. 1 (d). We can also see that for a nonlinear model, such as the Local\_SRO model introduced in the following section, the speedup will be reduced by a factor of 50, due to the aforementioned necessity of evaluating the local energies of each sites within the LIZ. If we increase the system size to one billion atoms, then the speedup of SMC with respect to DFT will be further increased by a factor of  $10^9$  to reach  $10^{34}$ , as highlighted in Fig. 1 (d). This analysis clearly demonstrates the exceptional performance of the SMC method for large-scale MC simulations.

In addition to theoretical estimations, we compare our work with selected prior studies on the atomistic simulation of high-entropy alloy (HEA) thermodynamics, as summarized in Tab. 1. To contextualize the simulation scale of our work, we extend our search beyond HEAs to identify the largest atomistic simulation system reported in the literature. A recent study achieved this with a system of 29 billion atoms, which employs 35 million CPU cores on one of the world's largest supercomputers (comprising 90,000 computing nodes, approximately 84% of the entire system). In contrast, constrained by computational resources, our work utilized only two Nvidia H-800 GPUs, yet achieved a simulation scale of one billion atoms. Note that this already surpasses the 100-million-atom system size of the 2020 Gordon-Bell Prize winner [22]. For HEAs, our work represents the largest system size achieved in atomistic simulations at ab initio accuracy. Furthermore, we demonstrate that, through careful design of the Monte Carlo (MC) algorithm to fully exploit its inherent parallelization potential, MC simulations can be scaled to billions of atoms, rivaling the scalability of molecular dynamics (MD) methods, which are traditionally viewed as more amenable to parallelization and large-scale

Materials	Simulation Method	Model	System Size (Atoms)	Subject	Ref.
MoNbTaW, MoNbTaWV, MoNbTaWTi	Canonical MC	EPI (6th-NN)	1,000	SRO, order-disorder transition	[33]
AlCoCrFeNi	Canonical MC	EPI (NN)	6,912	LRO and SRO, ordered multi-phase HEA	[56]
NiCoFeAlTiB	Semi-grand canonical MC	EPI (4th-NN)	32,000	Phase diagram, SRO and LRO	[29]
NbMoTaW	Hybrid MC/MD	SNAP	36,000	Grain boundaries (GBs) and SRO	[57]
MoNbTaW	Hybrid MC/MD	MTP	573,672	Dislocation motion under SRO	[58]
<b>FeCoNiAlTi, MoNbTaW</b>	<b>Canonical MC</b>	<b>EPI (2nd-NN) + nonlinear ML model</b>	$1 \times 10^9$	<b>Nanostructures (size, composition, and morphology)</b>	<b>This work</b>
Water/Copper Systems	MD	DeepMD	$29 \times 10^9$	Performance benchmark on an exascale supercomputer with 35-M CPU cores	[59]

Table 1: Comparison of our work with selected prior studies employing atomistic simulations in high-entropy alloys. For reference, we also include the largest atomistic system (29-B) simulated using machine learning (ML) models, as identified in the literature. Notably, Ref. [59] utilized 35 million CPU cores in one of the world’s fastest supercomputers, whereas this work achieved billion atoms using only two Nvidia H-800 GPUs.

simulations. Second, we highlight that, due to limitations in accessible system sizes, no prior work has addressed the challenge of modeling nanostructures in HEAs, particularly when the feature size of these nanostructures requires millions of atoms for accurate description. Our capability not only underscores the strength of our method but also addresses a critical gap in the field, as nanoparticles[40, 47, 54, 39] and nonphases [55] play a pivotal role in the design of HEAs with superb mechanical properties, such as overcoming the trade-off in strength and ductility [55, 39].

## 2.2. Energy model

In this work, we focus on two types of energy model: effective-pair-interaction (EPI) model [60, 48], and a nonlinear model that uses the local SRO parameter as the input feature. The EPI model is a generalized Ising model that is constructed via machine learning from the DFT data. By automatically selecting the interaction range via Bayesian information criterion (BIC) [48], the EPI model demonstrates that it can predict the DFT-calculated configuration energies of a series of HEAs with very high accuracy and has been applied to

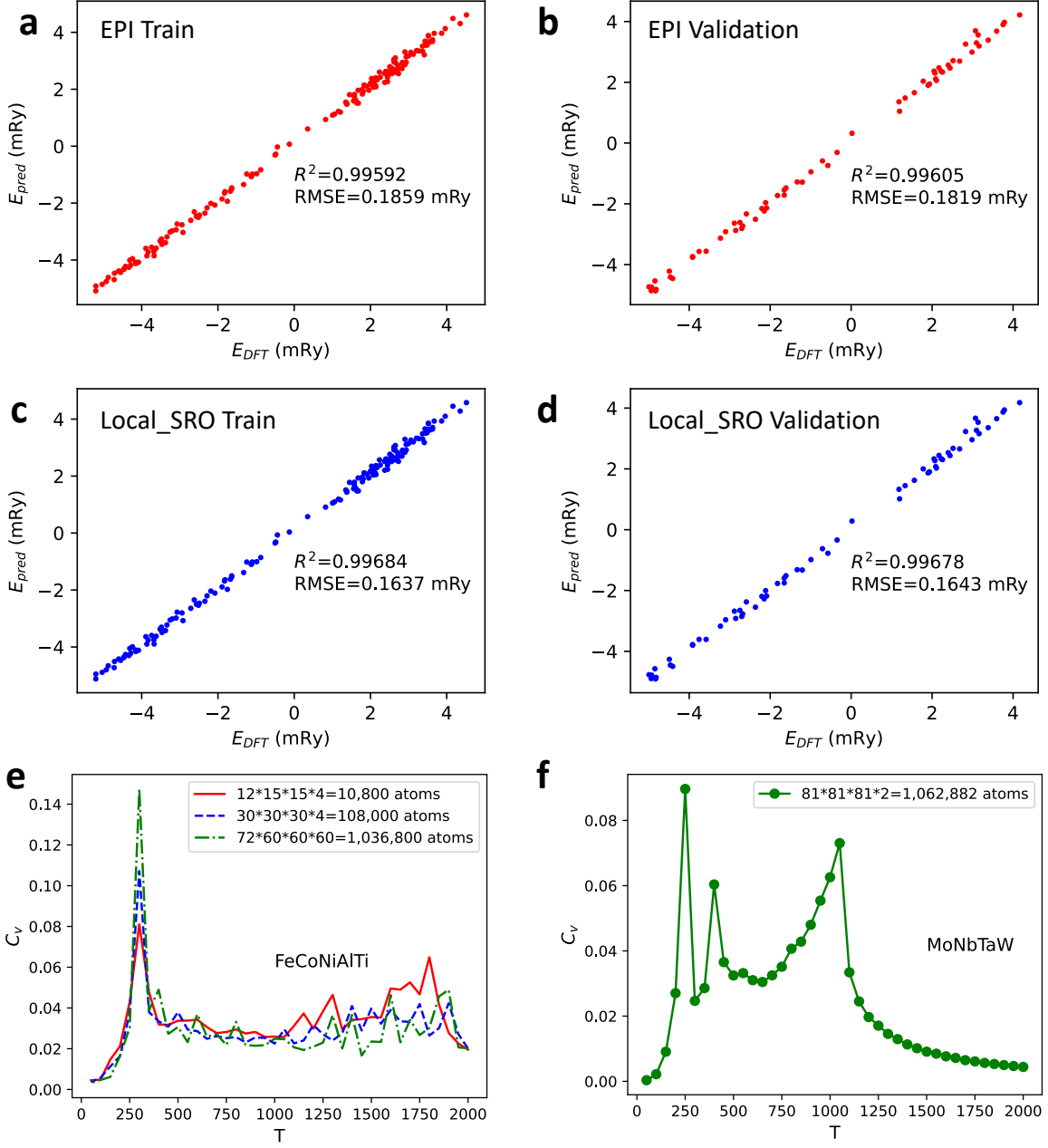


Figure 2: The accuracy of the energy model and the calculated specific heats for FeCoNiAlTi and MoNbTaW. (a) The training error of the EPI model for FeCoNiAlTi. (b) The validation error of the EPI model for FeCoNiAlTi (0.7/0.3 train-validation splitting). (c) The training error of the local\_SRO model for FeCoNiAlTi. (d) The validation error of the local\_SRO model for FeCoNiAlTi. (e) The specific heats  $C_v$  of FeCoNiAlTi calculated with different supercell sizes. (f) The specific heats of MoNbTaW calculated with a 1 million atom supercell.

study the order-disorder transitions in HEAs [33]. The local-SRO model, on the other hand, generalizes the EPI model by adding a quadratic term. As will be shown in the following discussion, this simple nonlinear term has a profound impact on the computing pattern, and

serves as a prototype for more involved machine learning models. A detailed description of the two energy models are present in the Method 3.2.

Using a train-validation splitting of 70% and 30%, we evaluated the accuracy of the second-nearest-neighbor (2nd-NN) EPI model and the loca\_SRO model and the results are shown in Fig. 2 (a-d). Both models are trained with the Adam optimizer and back-propagation algorithm, as will be detailed in the method section. It can be seen that both of the two models demonstrates very high accuracy. For the EPI model, the validation root-mean-square-error (RMSE) is 0.1819 mRy, or approximately 2.5 meV, which is well within quantum chemical accuracy (approximately 3.16 mRy/atom), as well as smaller than the typical errors of 5–12 meV/atom in the DFT methods [61]. The local\_SRO model demonstrates slightly higher accuracy than the EPI model, with a validation RMSE of 0.1643 mRy/atom, which can be attribute to its inclusion of high-order interactions. The high accuracy of the models is also demonstrated in the  $R^2$  scores, which are all higher than 0.995. The errors from the train and validation datasets are also very close to each other, indicating the absence of overfitting in the models. For comparison, we notice that this accuracy is higher than that in Ref. [29], which reported as 14.7 meV/atom by applying a similar pair-interaction model in the FeCoNiAlTiB system. We believe one reason for the enhanced accuracy is our approach to obtain the DFT dataset, which combines both random configurations, as well as configurations from Monte Carlo simulations, as described in Ref. [33].

Using the trained models, we calculated the specific heats  $C_v$  in the FeCoNiAlTi HEA in temperatures range from 50 K to 2000 K. The results are shown in Fig. 2 (e). It can be seen that there is a sharp order-disorder transition at a low temperature of about 300 K. The sharp peak evolves to singularity with the increase of the system size, which signifies the occurrence of a first-order transition. We also calculated the  $C_v$  curve for the MoNbTaW refractory HEA. The results in Fig. 2 (f) agree well with the results in Ref. [33], which are calculated using a small system of 1000 atoms. While the order-disorder transition at lower temperatures (between 250 K and 500 K) in the  $C_V$  curve cannot be directly compared with experiments due to the ignorance of kinetic barrier effects in the lattice MC method, the results at elevated temperatures are more suitable for comparison if experimental data are available, as demonstrated in Ref. [34]. A comparison of Fig. 2 (e) and (f) in the temperature range between 500 K and 2000K shows an interesting difference between the two HEAs: The  $C_v$  curve in  $\text{Fe}_{29}\text{Co}_{29}\text{Ni}_{28}\text{Al}_7\text{Ti}_7$  is generally flat, but demonstrates clear fluctuation as the temperature changes. By comparison, the  $C_v$  curve of MoNbTaW in the same temperature region is smooth, but with an obvious order-disorder transition around 1000 K (the exact location depends on the energy model and different values have been reported in various theoretical works [62, 28, 33, 63]). We think that such a difference originates from their

distinct chemical concentrations:  $\text{Fe}_{29}\text{Co}_{29}\text{Ni}_{28}\text{Al}_7\text{Ti}_7$  is nonequimolar while  $\text{MoNbTaW}$  is equimolar. In equimolar systems, the ordered phase often has a well-defined stoichiometry (e.g., AB in a binary alloy). The transition between ordered and disordered phases is typically sharper and more likely to be first-order. In non-equimolar systems, the ordered phase may deviate from ideal stoichiometry, leading to defects or partial ordering. We will present more results in the following discussion of the nanostructures.

### 2.3. Nanostructures in $\text{FeCoNiAlTi}$

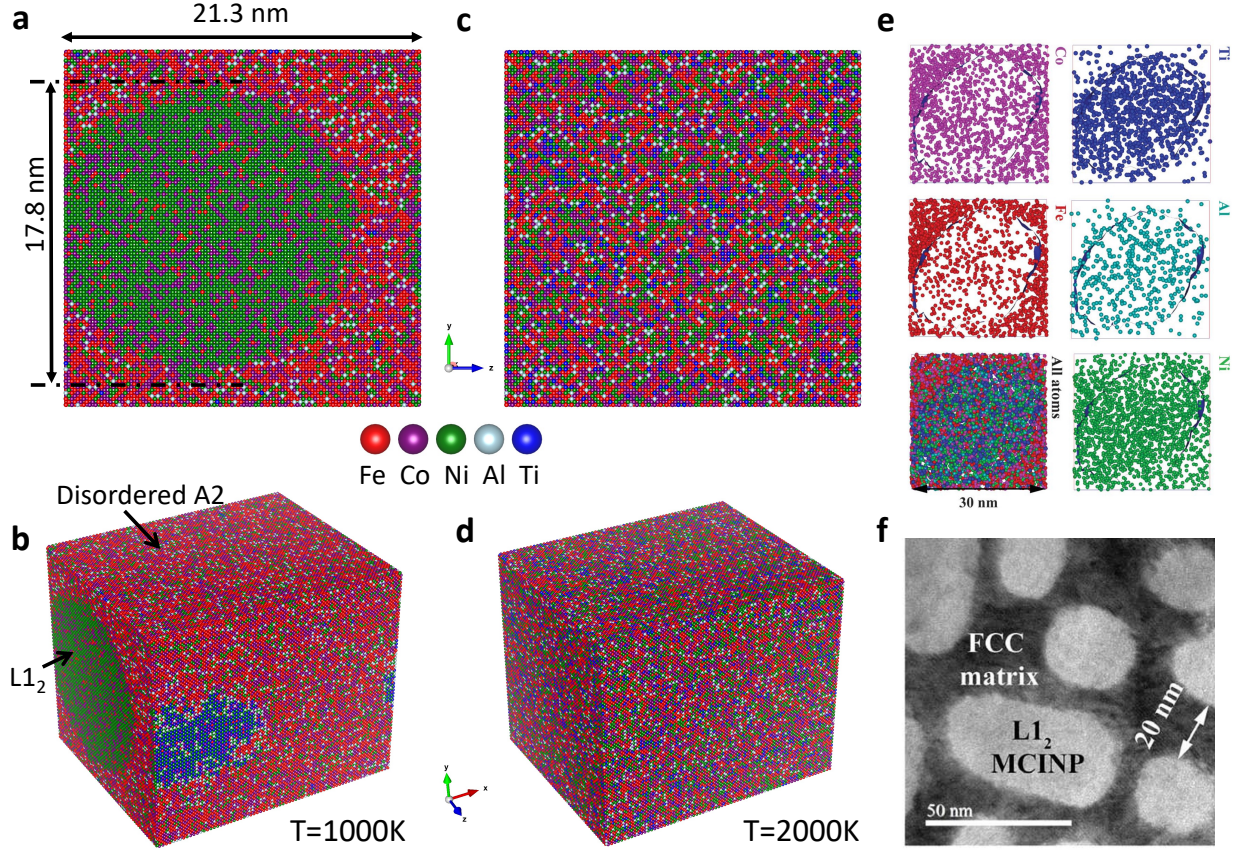


Figure 3: Simulation results for  $\text{FeCoNiAlTi}$  with 1 million atoms. (a) A snapshot of the the (001) face at 1000 K. (b) a perspective 3D snapshot of the configuration at 1000 K, from the signified direction (c) A snapshot view of the (001) face at 2000 K (d) a 3D view of the configuration at 2000 K. (e) High-resolution atom maps showing the atomistic distribution within the  $\text{L1}_2$  nanoparticles of the  $\text{Al}_7\text{Ti}_7$  alloy. Reproduced from Fig. 2 in Ref. [39]. (f) TEM image of the  $\text{Al}_7\text{Ti}_7$  alloy showing the nanostructured morphology. Reproduced from Fig. 1 in Ref. [39] with reprint permission from Science.

Using the local SRO model, we first simulated the chemical phase changes of the  $\text{Fe}_{29}\text{Co}_{29}\text{Ni}_{28}\text{Al}_7\text{Ti}_7$  fcc alloy using a supercell of approximately one million atoms. This alloy has demonstrated exceptional combined strength and ductility in experiment, and this attractive property has been attributed to the formation of nanoparticles in the  $\text{FeCoNi}$  matrix [39]. In experiment,

the alloy sample is homogenized at  $1150^{\circ}C$  (1423 K) for 2 hours and aged at  $780^{\circ}C$  (1053 K) for 4 hours. In the canonical MC simulation, the lattice dimension is chosen as  $72 \times 60 \times 60$ , therefore, the total number of atoms is  $72 \times 60 \times 60 \times 4 = 1,036,800$ . We initialize the configurations randomly at 2000 K, then decrease the simulation temperature by 50 K each time till 1000 K, which is approximately the temperature that the samples being aged. At each temperature, we skip  $4 \times 10^5 - 1.5 \times 10^6$  MC sweeps before recording the following 20,000 sweeps for calculating the specific heats  $C_v$  in Fig. 2 (e). The configurations at 2000 K and 1000 K are demonstrated in Fig. 3. It can be seen that the system is close to random at 2000 K. As the temperature decreases to 1000 K, the nanoparticles stabilize. The distribution of elements in the nanoparticle, as shown in Fig. 3 (a-b), reveals that it forms a slightly randomized A3B  $L1_2$  structure, with Ni and Co occupying the A sites primarily, Al and Ti occupying the B sites and Fe can occupy either A or B sites. This agrees well with the experimental results in Ref. [39], as reproduced in Fig. 3 (e-f). The diameter of the cluster shown in Fig. 3 (a) is about 17.8 nm, which is in agreement with the experimental observation shown in Fig. 3 (f). Similar results are also reported in Ref. [64] for the  $Fe_{25}Co_{25}Ni_{25}Al_{15}Ti_{10}$  HEA, where the fcc phase consisted of a  $\gamma$  Fe-(Co,Ni)-based solid-solution matrix (A1), and coherent primary  $\gamma'$  (Ni,Co)3-(Ti,Al)-based intermetallic  $L1_2$  precipitates.

From Fig. 3, it is obvious that even the 1 million-atom supercell is not large enough for studying the nanostructures in the FeCoNiAlTi HEA. To investigate the microstructures of the FeCoNiAlTi HEA at larger length scale, we employ a  $630 \times 630 \times 630$  fcc supercell, in which the total number of atoms is 1,000,188,000. Due to the huge supercell size, we use the faster EPI model rather than the local SRO model. Similar to the 1M atoms case, we evenly decrease the simulation temperature from 2000 K to 1000 K using a step of 50 K. For the 1B atom system, we no longer record the MC configurations and run  $10^5$  MC sweeps before recording the configuration at  $T = 1000$  K. Note that, generally speaking, the  $10^5$  number of MC sweeps is not large enough for a supercell as large as one billion atoms to reach thermal equilibrium, so the simulation is closer to simulated annealing. Nevertheless, this nonequilibrium does not necessarily present as a problem since the actual synthesis of alloys is typically a nonequilibrium process involving rapid heating-cooling process, in which the phases at high-temperature can be trapped by kinetic barrier and be maintained to low temperature.

The simulation results for this one billion-atom system are presented in Fig. 4. To study the size, composition, and morphologies of the nanoparticles, we also employ the union-find algorithm to identify the nanoparticles, as will be detailed in the method sections. We refer to all sets of atoms identified by the union-find algorithm as clusters, which can be of sizes ranging from a single isolated atom to the whole matrix phase. We make a histogram of

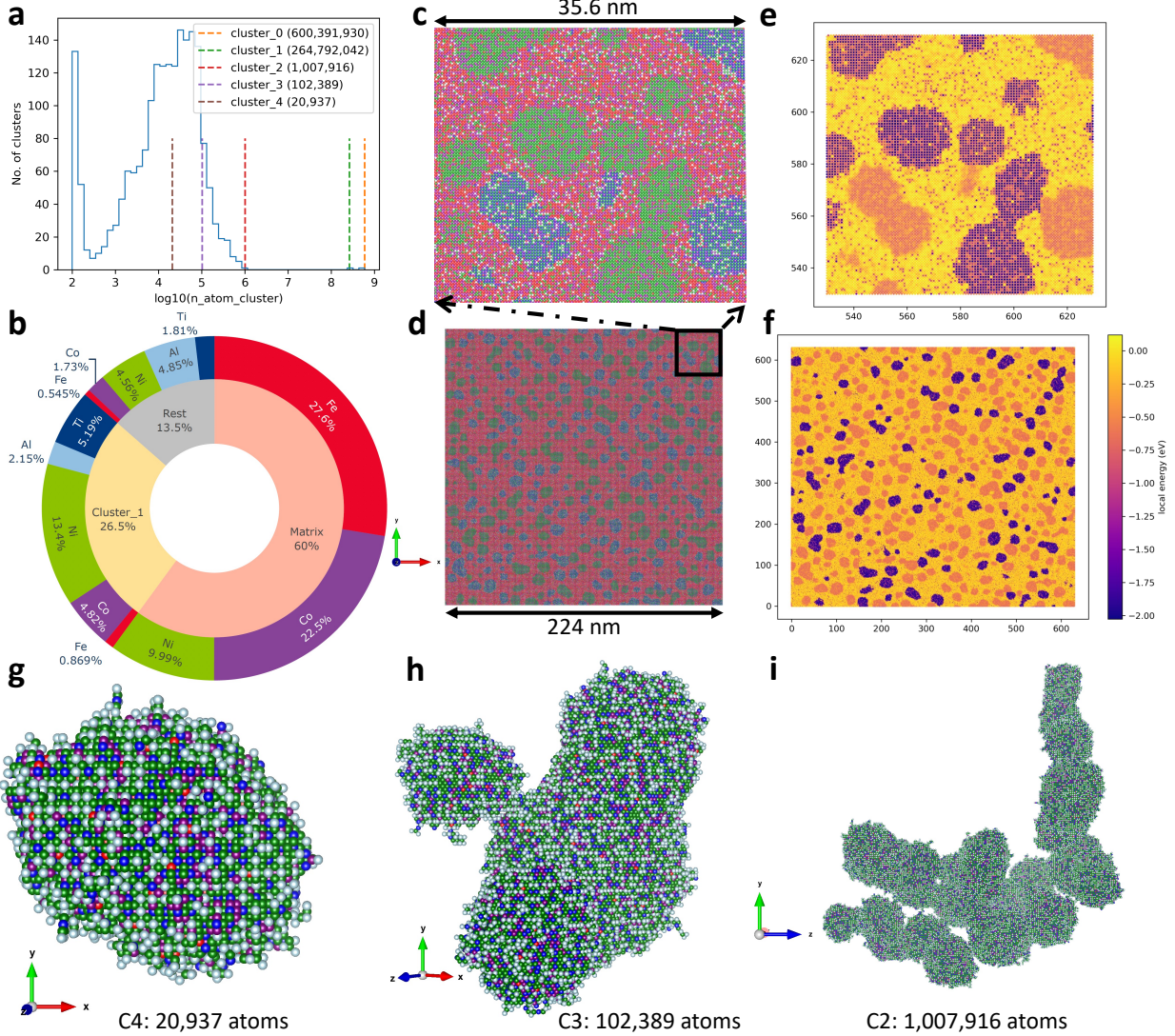


Figure 4: Comparing the simulated configurations of the 1 billion atom FeCoNiAlTi with the experimental results. (a) A histogram for all clusters of sizes larger than 100 atoms. Five clusters of different sizes are selected and shown as vertical dashed lines. (b) The chemical concentrations of the matrix (cluster\_0) and cluster\_1, as well as the rest clusters. (c-f) Snapshots of the [001] face of NiCoFeAlTi at T=1000K, with (c) as the enlarged upper-right corner of (d), and (e) as the enlarged upper-right corner of (f). (c-d) show the different elements, and (e-f) show the atomic local energies. (g-i) 3D snapshot of cluster\_4, 3, and 2, respectively.

all clusters of sizes larger than 100 atoms in Fig. 4 (a). It can be seen that the largest one is cluster\_0, which contains about 0.6 billion atoms. This is the matrix phase, which contains only Fe, Co, and Ni, as demonstrated in Fig. 4 (b). Note that the absence of Al and Ti atoms in cluster\_0 is a result of the union-find algorithm, which automatically identifies isolated Al and Ti atoms in cluster\_0 as individual clusters of size one. From Fig. 4 (c), we see that the FeCoNi matrix phase is a disordered A1 structure. The cause of the disorder

can be seen from Fig. 4 (e) and (f), which show the local energies of each atom with the color bar. It can be seen that in the matrix phase, the local energies of different atoms are generally close to each other, which means that the Fe, Co, and Ni atoms have no significant site preferences. On the other hand, the nanoparticles, which forms  $L1_2$  structure as shown in Fig. 4 (c), contains sites with much lower atomic local energies, as shown in Fig. 4 (e). In fact, the local energy difference is exactly the criteria we make use of to distinguish the matrix and nanoparticles, as described in Method 3.4. The FeCoNi matrix phase is the entropy-stabilized disordered phase, while the  $L1_2$  phase is the enthalpy favorable ordered phase. In other words, the occurrence of both disordered A1 structure and ordered  $L1_2$  structure is a result of the competition between the entropy and enthalpy contributions in the free energy.

To study the size, compositions, and morphologies of the nanoparticle in more detail, we choose four representative nanoparticles, as illustrated in Fig. 4 (a) as cluster\_1, 2, 3, and 4, which have sizes of 264,792,042, 1,007,916, 102,389, and 20,937 atoms. Their chemical concentrations are also listed in Tab. 2, which aligns excellently with the experimental results [29]. From Fig. 4 (a), we note that the peak of the histogram is at about  $10^5$  atoms, which corresponds to a cluster of 29 atoms, or 10.3 nm in diameter. For cluster\_1, similar calculation gives a value of 22.0 nm in diameter, if we assume that the particles are spherical. However, inspecting the 3D morphology of the clusters reveals that they are actually not all simple spheres, as shown in Fig. 4 (g-i): While sphere is a good approximation for the smaller cluster\_4, the larger cluster\_3 and cluster\_2 are both comprising of multiple nanoparticles, which indicates that the smaller nanoparticles can merge together to form larger ones, as shown by the dendritic structures at the surface of the nanoparticles. In fact, from Fig. 4 (a,b) we see that the largest  $L1_2$  cluster: cluster\_1, contains a total of more than 264 million atoms, which accounts for 66% of the atoms in the nonmatrix phases. In other words, most of the nanoparticles shown in Fig. 4 (c-f) are actually connected at 3-dimension and are parts of cluster\_1. While this theoretical observation of 3D-connected nanoparticles still demands experimental verification, we highlight that it seems likely considering the high density of nanoparticles observed in the experiment [39], which results from the chemical complexity in HEAs. We further argue that, if the nanoparticles are indeed connected, it can significantly impact the motion of dislocations, which then have to go through the ordered nanoparticles rather than circumvent them. Other than the mechanical properties, the morphology of the nanoparticles also have important application in catalysis, which would be an interesting topic for future research.

	Ni	Co	Fe	Al	Ti
$L1_2^{EXP}$	43.23	23.69	10.06	8.61	14.41
Matrix $^{EXP}$	18.69	31.84	41.13	5.69	2.66
Matrix $^{MC}$	16.64	37.41	45.96	0.0	0.0
Cluster $_1^{MC}$	50.8	18.2	3.28	8.11	19.61
Cluster $_2^{MC}$	50.77	18.26	3.32	8.01	19.63
Cluster $_3^{MC}$	50.72	18.25	3.28	8.15	19.6
Cluster $_4^{MC}$	50.51	17.92	3.38	8.55	19.64

Table 2: Comparison of the experimental values [29] with our simulation results for the compositions of the matrix and four representative  $L1_2$  clusters, as listed in Fig. 4. Note that Matrix $^{MC}$  is Cluster\_0. Due to the adoption of the union-find algorithm, the isolated atoms are automatically removed from the identified clusters, which is the cause of no Al and Ti atoms in the extracted matrix phase.

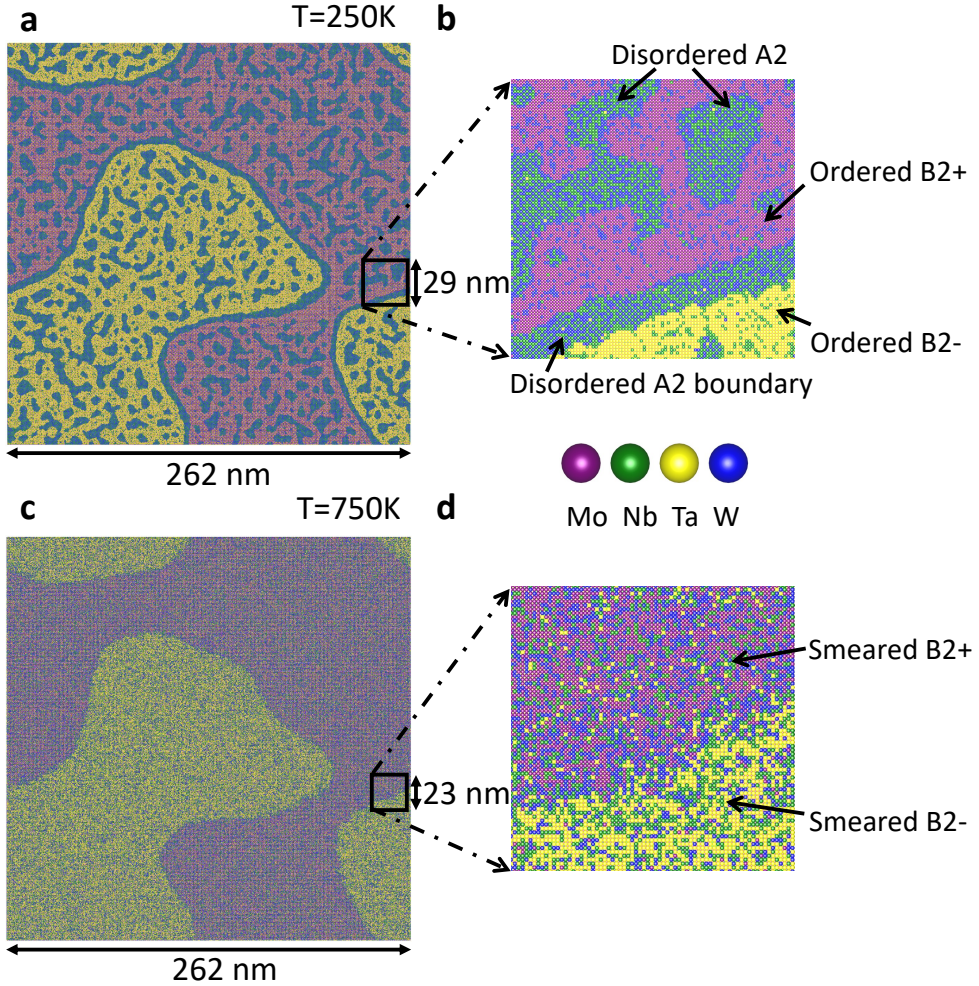


Figure 5: Simulation results for MoNbTaW with 1 billion atoms. (a) Snapshot of the [001] face at  $T=250\text{ K}$ . (b) A magnified view of the  $29\text{ nm}$  square in a. (c) Snapshot of the [001] face at  $T=750\text{ K}$ . (d) A magnified view of the  $23\text{ nm}$  square in c.

## 2.4. Nanostructures in $\text{MoNbTaW}$

Other than  $\text{FeCoNiAlTi}$ , we also employs our method to study the nanostructure evolution of a well-studied bcc HEA:  $\text{MoNbTaW}$ . The size of the supercell is  $795 \times 795 \times 795 \times 2 = 1,004,919,750$  atoms. The size of the link-cell is  $3 \times 3 \times 3$ , and the energy model is 2nd-NN EPI. The simulation temperatures decrease from 2000 K to 250K, with an temperature interval of 50 K. For each temperature we run the simulation for 30,000 sweeps. The simulation results is shown in Fig. 5. For  $T=250\text{K}$ , we can note from the figure is that there are two types of nanostructure: The smaller ones are mainly made up of Nb and Ta, and of a feature size of about 10 nm. It can be seen that the distribution of Nb and Ta elements within relatively random. The shape of these small nanoparticles are also more diverse than that in the  $\text{FeCoNiAlTi}$ . Other than the small nanostructure, there are also larger nanophases of a feature size of about 100 nm, which is at the same length scale as the supercell. The two nanophases are shown as yellow and purple in the figure. It is easy to see that they are actually the  $\text{NbW B2}$  phases. The difference between the yellow and the purple nanophase is that one of them have Ta occupies the center position of the perfect bcc lattice, while the other has Mo occupies the center site. Therefore these two nonophases just correspond to a spontaneous symmetry breaking of an Ising model along either the plus or the minus directions. At  $T=250\text{ K}$ , a chemical grain-boundary made up of Nb and Ta can be clearly seen between the two nanophases, and the thickness of the chemical grain boundary is about 3 nm. As the temperature increases to 750 K, it can be see that the larger nanophases still exist, which means that those features are more stable against thermal fluctuations. On the other hand, the smaller nanoparticles vanish, along with the chemical grain boundary between the yellow and purple nanophases. The stability of the nanophases presents an interesting phenomenon, which we propose to explain as follows: at low temperatures, the chemical grain boundary acts as a protective barrier, preventing the formation of energetically unfavorable AA or BB nearest-neighbor pairs when the two nanophases come into contact. On the other hand, as the temperature increases, despite the vanish of the chemical grain boundary, the two nanophases also are no longer perfect B2 structures. This disorder reduces the energy cost at the boundary, allowing the nanostructures to persist even in the absence of the protective chemical grain boundary. It would be intriguing if this “disorder-protected phase” observed in our simulations could be directly verified experimentally.

## 3. Method

### 3.1. Implementation of $\text{SMC\_GPU}$

For a simple nearest-neighbor 2D Ising model, a widely used parallelization scheme is the checkerboard algorithm. In the checkerboard algorithm, the 2D square lattice is divided

into two sublattices, one colored black and the other white. Note that the lattice sites of the same color will not interact with each other, therefore the sites of one color can be updated simultaneously by fixing the sites of the other color. The checkerboard algorithm is very efficient and has been applied to study the 2D and 3D Ising models on different accelerators, including GPU [35, 65, 66], TPU [67], and FPGA [68, 69].

The checkerboard algorithm cannot be directly applied when the Hamiltonian contains interactions beyond the nearest neighbors. Therefore, it is rarely used for studying real materials, where the interaction range is typically beyond nearest neighbors. For such a purpose, a generalization of the checkerboard algorithm can be employed to harness the move-parallelism opportunity. This method is referred to as parallelized link-cell algorithm [70]. In link-cell algorithm, the lattice is decomposed into  $N$  cells of fixed size  $a_{cell}$ , which should be larger than the interaction range. With link-cell algorithm, the serial MC code can be accelerated by up to  $N$  times. For a multi-GPU system, the  $N$  cells are evenly distributed on all the GPUs, and ghost boundaries are added to take into account the interactions between atoms from different GPUs, as shown in the right part of Fig. 1.

- Parallelization implementation: The actual parallelization implementation on GPUs depends on the energy model. For pairwise model such as EPI, the iteration over the  $i_C$  index is executed in parallel as CUDA threads on GPU. For more general energy models such as the local\_SRO model, the  $i_C$  index is parallelized in the CUDA blocks dimension, and the calculation of the local energies for each sites within LIZ is parallelized with the CUDA threads, as demonstrated in the flowchart in Fig. 6.
- Link-cell size: Using the link-cell algorithm, the one MC sweep (MC trials over every sites) is decomposed into  $n_A$  sequential steps, with each one of  $n_C$  parallel moves. For instance, for a  $300 \times 300 \times 300$  bcc supercell (a total of  $300^3 \times 2 = 54,000,000$  atoms), assuming next-to-nearest-neighbor interaction, then the link-cell length can be chosen as  $3 \times a$ , where  $a$  is the lattice constant. The link-cell size  $n_A$  is  $3 \times 3 \times 3 \times 2 = 54$ , and the number of link-cell is  $n_C = 1,000,000$ .
- Random number generator: An efficient random number generator is important for MC simulation because random numbers are needed for every MC trial, as shown in the fourth and fifth steps in Fig. 6. Our implementation makes use of the NVIDIA CUDA Random Number Generation library (cuRAND), which delivers high performance GPU-accelerated pseudorandom numbers.
- Search neighbors: Another important consideration is how to efficiently find the neighboring sites, for which their chemical species need to be read from the memory, as

shown in the third step in Fig. 6. In practice, we make use of the lattice structure and directly calculate the indices of the neighbors for a specific atom on-the-fly using a list of the relative positions of the neighboring atoms. This method has a constant time complexity, which is advantageous over the more common practice of using k-D tree to store the atomic positions and search the neighbors, which has time complexity of  $O(\log(N))$ .

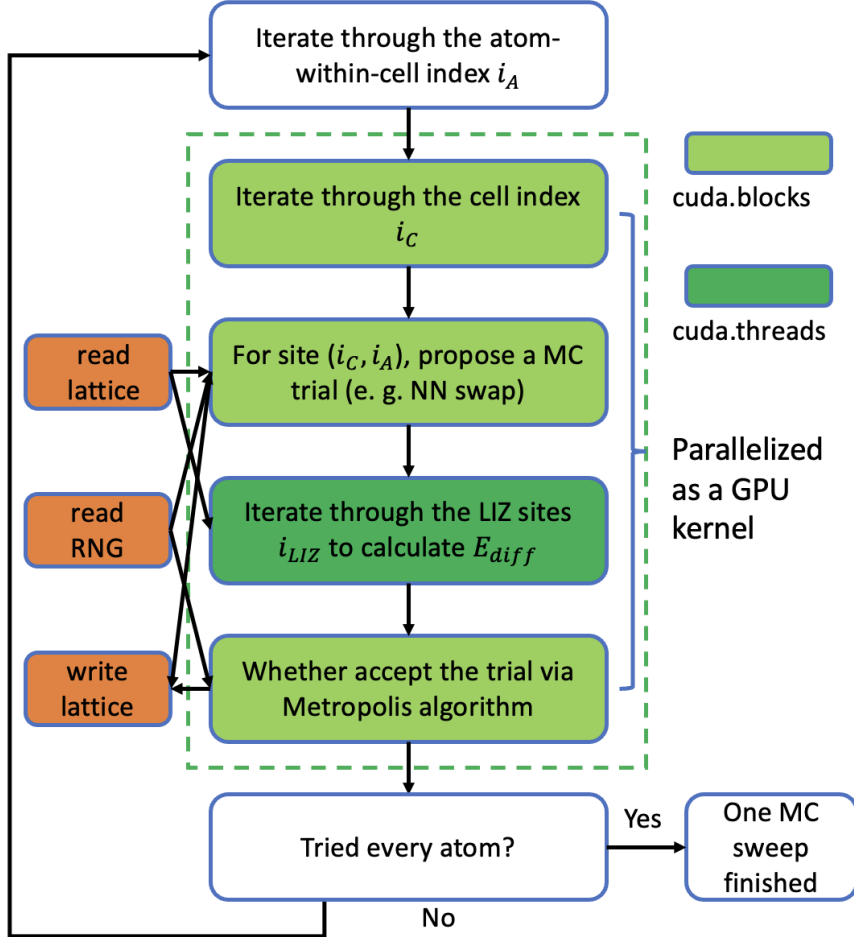


Figure 6: A schematic flowchart for the link-cell parallelism algorithm for a machine learning energy model. The outer loop over index  $i_A$  are executed sequentially, while the inner loop over index  $i_C$  are executed in parallel as a CUDA kernel since the MC update atoms of the same  $i_A$  index but different  $i_C$  indices are independent.

### 3.2. The EPI and Local\_SRO model

In the EPI model, the effective Hamiltonian of the system is made up of chemical pair interactions of the centering atom with neighboring atoms within some cutoff radius. The local chemical environment is specified by  $\vec{\sigma} = (\sigma^0, \sigma^1, \dots, \sigma^{N_n-1})$ , which denotes the chemical

species of the  $N_n$ -th neighboring atoms. The local energy  $E_i$  is given by

$$E_i = \sum_f V^f \pi^f(\vec{\sigma}_i) + V_i^p + V^0 + \epsilon, \quad (2)$$

where  $\epsilon$  is the uncertainty of the EPI model,  $V^0$  is the bias term same for all sites,  $V_i^p$  is a single-site term depending only on the chemical component  $p$  of atom  $i$ ,  $V^f$  are the EPI parameters, and  $\pi^f$  are the number of pair interactions of type  $f$ . The feature index  $f$  is actually made up of three parts  $(p, p', m)$ , representing the element of the local atom, the element of the neighboring atoms, and the coordination shell, respectively. For a canonical system, summing up the local energies over all sites, the total energy is then given by

$$E = N \sum_{p' < p, m} V_m^{pp'} \Pi_m^{pp'} + \text{const} + \epsilon, \quad (3)$$

where  $N$  is the total number of atoms and  $\Pi_m^{pp'}$  is the proportion of  $pp'$  interaction in the  $m$ -th neighboring shell. Note that due to the fixed chemical composition in canonical system, the single-site term  $V_i^p$  has been absorbed into the constant, and the number of independent EPI parameters is  $M(M-1)/2$  for a  $M$ -component system, which is the reason for the  $p' < p$  requirement. In practice, the EPI parameters are determined via Bayesian regression [33].

As mentioned, since the EPI model contains only pairwise interactions, the calculation of the energy changes after a MC swap trial is simple: we simply multiply the local energy changes of the two swapping sites by a factor of 2 to take into account the local energy changes of other sites. For more general energy models that contain higher-order/nonlinear interactions, the total energy changes need to be explicitly calculated by adding up the local energies of all sites within the LIZ. As a demonstration of our method for more general machine learning models, here we modify the EPI model by adding a simple quadratic term, and the local energy for each site  $E_i$  is:

$$E_i = \sum_{p' < p, m} V_m^{pp'} \pi_m^{pp'} + \sum_{p, m} W_m^p (\pi_m^{pp})^2 + \lambda \sum_{p, m} (W_m^p)^2 + \text{const} + \epsilon, \quad (4)$$

in which

$$\pi_m^{pp'} = \frac{n_m^{pp'}}{\sum_{pp'} n_m^{pp'}} \quad (5)$$

is the percentage of  $pp'$  interactions for the  $m$ 's coordination shell, and  $n_m^{pp'}$  is the number of pairs with index  $(m, p, p')$ . Note that we limit the quadratic interaction to the same-element

pairs to reduce the number of higher-order terms. The third term on the right of Eq. 6 is a  $l^2$  regularization of the weights of the quadratic term, reflecting our prior that the higher-order interactions should be a small correction to the EPI model. We name it as the local SRO model since  $\Pi_m^{pp'}$  describes the short-range order within the local chemical environment. It should be noted that unlike EPI, this local SRO model is no longer a linear, or even quadratic function of the pairwise interactions. Instead, it can be expressed as a power series (infinite degree polynomial) of the pairwise interactions due to the  $(\pi_m^{pp'})^2$  term. This is also the reason we do not refer to it as “quadratic EPI model”. It is easy to see that the nonlinear interactions can also be modeled with neural networks such as the multilayer perceptrons:

$$E_i = \sum_{p' < p, m} V_m^{pp'} \pi_m^{pp'} + \text{MLP}(\pi_m^{pp'}) + \epsilon. \quad (6)$$

However, due to the large number of principal elements, the number of parameters in such MLP model can easily go beyond the number of data points used in this work (e.g. 220 for FeCoNiAlTi), which lead a high risk of overfitting. Therefore, in this work we will use the local SRO model as a representation of general ML energy models, and leave more complex models for future study when significantly larger DFT datasets are available.

### 3.3. DFT dataset

We use the LSMS method [50] to calculate the total energy of the system. LSMS is a all-electron electronic structure calculation method, in which the computational cost scales linearly with respect to the number of atoms. For FeCoNiAlTi, we use a 100 atom supercell with a lattice constant of 6.72 Bohr (0.356 nm). We employs spin-polarized scheme to account for the magnetic interactions in the system. The angular momentum cutoff  $l_{max}$  for the electron wavefunctions is chosen as 3, and the default LIZ cutoff radius is chosen as 12.5 Bohr. We used PBE as the exchange-correlational functional. To enhance the representativeness of the DFT data, the total dataset is made up of 120 random generated configurations and 100 configurations from Monte Carlo simulation, as proposed in Ref. [33]. Therefore the total number of configurations is 220, with each one comprising 100 atoms.

For MoNbTaW, the DFT dataset has been reported in Ref. [33], which is also made up of the random samples and the MC samples. The 704 random samples are calculated with supercells of 64, 128, 256, and 512 atoms. The 72 MC samples are obtained from MC simulations at different temperatures, on a 1000-atom supercell. When calculate the energies of the MoNbTaW system, the lattice constant is set at 6.2 Bohr, and the angular momentum cutoff is chosen as 3. The Barth-Hedin local-density approximation are used as the exchange-correlation functional. The local interaction zone (LIZ) is maintained at

59 atoms. To adequately capture the effects of heavier elements in the system, the scalar-relativistic equation is used instead of the conventional Schrödinger equation.

### 3.4. MC simulation

System_Model	Dimensions	Link-cell	T <sub>sweep</sub> (s)	N <sub>sweeps</sub> /T
FeCoNiAlTi_1M_EPI	72 × 60 × 60 × 4	3 × 3 × 3	0.001755	$1.5 \times 10^6$ (1000 K)
FeCoNiAlTi_1M_LocalSRO	72 × 60 × 60 × 4	4 × 4 × 4	0.04703	$10^5$ (1000 K)
FeCoNiAlTi_1B_EPI	630 × 630 × 630 × 4	3 × 3 × 3	0.4120	$10^5$ (1000 K)
FeCoNiAlTi_1B_LocalSRO	632 × 632 × 632 × 4	4 × 4 × 4	21.65	$10^4$ (1000 K)
MoNbTaW_1B_EPI	795 × 795 × 795 × 2	3 × 3 × 3	0.1912	$10^5$ (50 K)

Table 3: The MC simulation results obtained with different systems and models. The dimensions are made up of  $nx \times ny \times nz \times m$ , where  $nx, ny, nz$  are the supercell vectors along the  $x, y, z$  direction, and  $m$  is the number of atoms in the cubic cell.

The results shown in this work are based on five simulation results using different model and systems, as shown in Tab. 3. The MC simulation is a simulated annealing process in the canonical ensemble (NVT). The temperature is initialized as 2000 K and then decrease with a step of 50 K. The initial  $N_{\text{sweeps}}$  are discarded before making measurement or taking the snapshot of the configuration. The number of  $N_{\text{sweeps}}$  generally increases as the temperature decreases to account for the lower acceptance ratio of MC moves. For instance, for FeCoNiAlTi\_1M\_EPI, the number of sweeps is  $4 \times 10^5$  at 2000 K, then increase to  $1.5 \times 10^6$  at  $T = 1000K$ . In order to extract the nanostructures from the simulation results, we employs the union-find algorithm, which uses a tree structure efficiently manage and manipulate partitions of a set into disjoint subsets. In order to apply the union-find algorithm, we first calculate the local energy of each site, and set a threshold of the energy to determine whether two sites belong to the same set (cluster). Finally, we used VESTA [71] for the visualization of the 3D crystals and clusters.

## 4. Conclusions

- We introduce a Scalable Monte Carlo (SMC) method that overcomes the parallelization bottlenecks inherent in conventional Monte Carlo (MC) simulations. By generalizing the checkerboard algorithm through the introduction of link cells, our approach reduces the computational complexity of an MC sweep from  $O(N^2)$  to  $O(N)$ . This method is not only applicable to pairwise interactions but also extends to nonlinear local interactions through the introduction of a local interaction zone, making it highly compatible with machine learning (ML)-enhanced atomistic models.

- The GPU accelerated implementation of the SMC method enables the simulation of atomistic systems exceeding one billion atoms while maintaining the accuracy of density functional theory (DFT). Such unprecedented capability makes it possible for us to directly observe the nanostructures in HEAs, which can be of more than millions of atoms and are vital for the superb mechanical properties in HEAs.
- Using the SMC-GPU code, we investigated two types of high entropy alloys that have demonstrated exceptional mechanical properties. For the fcc FeCoNiAlTi alloy, we identified that at the experimental aging temperature, nanoparticles of sizes about 10-20 nm will form within the random matrix. The nanoparticles forms a slightly randomized  $L1_2$  structure, with Ni and Co mainly occupies the A sites, and Al Ti mainly occupies the B sites. This size and composition of the nanoparticles agree excellently with the experimental findings [39]. Morover, we find that seemingly separate grains may, in fact, be connected, highlighting the intricate nature of high-entropy alloys (HEAs) and prompting a reconsideration of traditional grain size measurement methods.
- We further investigated the bcc MoNbTaW high-entropy alloy (HEA) using a one-billion-atom supercell. Our results reveal the formation of hierarchical nanostructures. The smaller nanoparticles consist of a disordered A2 structure comprising Nb and W, with a feature size of approximately 10 nm, and are observed exclusively at low temperatures. In contrast, the larger nanophase exhibits a B2 structure composed of Ta and Mo, with a feature size of about 100 nm. Interestingly, we find that the Ta-Mo B2 structures decompose into two distinct nanophases, B2+ and B2-, which are separated by a grain boundary enriched with Nb and W. Simulations suggest that the disordered Nb-W grain boundary acts as a protective barrier for the two nanophases as the temperature increases, which is an interesting theoretical phenomenon to be confirmed in experiment in the future.

## 5. Supplementary

### 5.1. Ising model

Ising model is a fundamental model in statistical mechanics [72]. The study of Ising model not only helps elucidating a plethora of important physics phenomena, such as ferromagnetic phase transition, renormalization-group, and critical behaviour [5], but also leads to the invention of many widely-used algorithms, such as the Swendsen-Wang algorithm [73], Wang-Landau algorithm [74], and Wolff cluster flipping algorithm [75, 76]. In the simplest form,

the Ising Hamiltonian can be written as:

$$H(\boldsymbol{\sigma}) = - \sum_{\langle i,j \rangle} J \sigma_i \sigma_j, \quad (7)$$

where  $J$  is the interacting parameter and  $\sigma_i$  represents the spin at the neighboring lattice site  $i$ , and  $\boldsymbol{\sigma}$  denotes a spin configuration in the lattice. Note that the summation is over all sites and their nearest neighbors. For example, in 2D square lattice, there are four nearest neighbors, and in 3D square lattice there are 6 nearest neighbors. It is also straightforward to generalize the above model to include longer-distance pair interactions within a predefined cutoff radius  $r_c$  in a general lattice. Such Ising-like models can then be applied to study real materials, in which the spin variable  $\sigma$  represents the different elements, and the generalized interaction parameters  $J_{\sigma_i \sigma_j}$  can be interpreted as the chemical bonding between atoms of specific elements.

### 5.2. Statistical mechanics

In statistical mechanics, the probability for the occurrence of configuration  $\boldsymbol{\sigma}_k$  is given by:

$$P(\boldsymbol{\sigma}_k) = \frac{e^{-\beta H(\boldsymbol{\sigma}_k)}}{Z}, \quad (8)$$

where the partition function is the sum of all the microstate probabilities:

$$Z = \sum_{\boldsymbol{\sigma}_k} e^{-\beta H(\boldsymbol{\sigma}_k)}, \quad (9)$$

and  $\beta = 1/(k_B T)$ , where  $k_B$  is the Boltzmann constant, and  $T$  is the temperature. After obtaining the partition function, physical observables  $\langle \hat{O} \rangle$  such as the expected energy, magnetization, specific heat, and magnetic susceptibility can then be calculated accordingly from

$$\langle \hat{O} \rangle = \sum_k \frac{O(\boldsymbol{\sigma}_k) e^{-\beta H(\boldsymbol{\sigma}_k)}}{Z}. \quad (10)$$

### 5.3. Monte Carlo Simulation Algorithms

A sample following the probability distribution of Eq. 8 can be generated via Markov chain Monte Carlo (MCMC) simulation. For such a purpose, different schemes can be devised, and the Metropolis-Hastings algorithms is among the most commonly used ones. For the Ising model in Eq. 7, the Metropolis-Hastings algorithm starts with proposing flipping

the spins of each lattice site. This trial move gives rise to a change of the total energy by  $\Delta E$ , and the acceptance probability of this trial is given by:

$$P = \begin{cases} 1, & \Delta E \leq 0 \\ \exp(-\beta\Delta E), & \Delta E > 0. \end{cases} \quad (11)$$

A Monte Carlo step, or sweep, is defined as attempting the above trial exactly one time for each lattice site. A Monte Carlo simulation typically starts with a given number of warm-up steps. These steps are needed for the system to reach thermal equilibrium. After that a measurement of the configuration is made for each step, and the results can be recorded to calculate the physical observables.

The Monte Carlo simulation can be carried out at different conditions, the most common ones are the canonical ensembles, grand-canonical ensembles, and semi-grand canonical ensembles. In canonical ensemble, the number of particles and the temperature is kept fixed. In the grand-canonical ensemble, the chemical potential is kept fixed, and the number of particles is determined by the equilibrium condition. The semi-grand canonical is a technique to fix the concentration of different elements by adjusting the value of the chemical potentials of each element. In this work, we focus on the canonical ensemble, which is relatively straightforward to implement. In a canonical Monte Carlo simulation, the first thing to note is that the flipping trial in Ising model is replaced with a swapping trial, in which a random pair of sites are chosen randomly to switch the particles.

#### 5.4. Parallelization opportunities in Monte Carlo simulation

Compared to molecular dynamics, Monte Carlo simulation is generally considered to be difficult for large-scale parallelization due to the sequential nature of the Metropolis updating. Nevertheless, there are still some parallelization opportunities that can be exploited. These opportunities can be generally divided into three groups:

- Temperature parallelism: the simulations at different temperatures are independent, therefore they are “embarrassingly parallel”. A closely related case is the replica exchange method, in which only the temperature of different replica need to be exchanged.
- Move parallelism: for two sites far-away from each other, the flipping or swapping move at one site won’t affect the energy of the other, due to the short-range nature of the interactions. This property can therefore presents a parallelization opportunity. Similarly, it is also possible to split a huge lattice to smaller ones, as long as the “ghost cells” at the boundary are taken care of.

- Sub-move parallelism: For calculating the energy change due to a single MC move, some fine-grain parallelization opportunities usually exist, depending on the form of the effective Hamiltonian. This is particularly true for the models based on neural networks, where the large number of matrix-multiplication operations present excellent opportunities for acceleration with highly optimized math libraries.

In this work, we focus our discussion on move-parallelism, since it is the bottleneck for large-scale MC simulation. Implementation of the temperature parallelism is straightforward. For sub-move parallelism, we make use of the fact that, in the general case, all the local energies of sites within a LIZ need to be evaluated, and the calculations of these local energies are independent of each other.

### **Data availability statement**

The data that support the findings in this study will be published upon the acceptance of this manuscript.

### **Acknowledgements**

The work of Xianglin Liu and Fanli Zhou was supported by the National Natural Science Foundation of China under Grant 12404283. The work of Yonghong Tian was supported by the National Natural Science Foundation of China under Grant Grant 62425101, 62088102. This work was also supported by the Pengcheng Laboratory Key Project (PCL2021A13) and utilized the computing resources of Pengcheng Cloud Brain.

### **Author contributions**

**Xianglin Liu:** Conceptualization, Methodology, Software, Funding Acquisition, Project Administration, Data Curation, Formal Analysis, Investigation, Visualization, Writing - original draft. **Kai Yang:** Software, Data Curation, Formal Analysis, Investigation. **Fanli Zhou:** Visualization, Writing - review & editing. **Yongxiang Liu:** Writing -review & editing. **Dengdong Fan:** Writing -review & editing. **Pengxiang Xu:** Resources, Funding Acquisition, Project Administration, Writing -review & editing. **Zongrui Pei** Formal Analysis, Writing -review & editing **Yonghong Tian:** Funding Acquisition, Writing -review & editing.

### *Corresponding authors*

Correspondence to Xianglin Liu (submitting) (xianglinliu01@gmail.com) or Pengxiang Xu (xupx@pcl.ac.cn)

## References

- [1] K. Burke, Perspective on density functional theory, *The Journal of Chemical Physics* 136 (2012) 150901.
- [2] D. Ma, B. Grabowski, F. Körmann, J. Neugebauer, D. Raabe, Ab initio thermodynamics of the cocrfemnni high entropy alloy: Importance of entropy contributions beyond the configurational one, *Acta Materialia* 100 (2015) 90–97.
- [3] S. N. Khan, M. Eisenbach, Density-functional Monte-Carlo simulation of CuZn order-disorder transition, *Phys. Rev. B* 93 (2016) 024203.
- [4] J. M. Sanchez, Renormalized interactions in truncated cluster expansions, *Phys. Rev. B* 99 (2019) 134206.
- [5] G. S. Pawley, R. H. Swendsen, D. J. Wallace, K. G. Wilson, Monte carlo renormalization-group calculations of critical behavior in the simple-cubic ising model, *Phys. Rev. B* 29 (1984) 4030–4040.
- [6] C. W. Park, M. Kornbluth, J. Vandermause, C. Wolverton, B. Kozinsky, J. P. Mailoa, Accurate and scalable graph neural network force field and molecular dynamics with direct force architecture, *npj Computational Materials* 7 (2021) 73.
- [7] S. Batzner, A. Musaelian, L. Sun, M. Geiger, J. P. Mailoa, M. Kornbluth, N. Molinari, T. E. Smidt, B. Kozinsky, E(3)-equivariant graph neural networks for data-efficient and accurate interatomic potentials, *Nature Communications* 13 (2022) 2453.
- [8] K. Song, R. Zhao, J. Liu, Y. Wang, E. Lindgren, Y. Wang, S. Chen, K. Xu, T. Liang, P. Ying, N. Xu, Z. Zhao, J. Shi, J. Wang, S. Lyu, Z. Zeng, S. Liang, H. Dong, L. Sun, Y. Chen, Z. Zhang, W. Guo, P. Qian, J. Sun, P. Erhart, T. Ala-Nissila, Y. Su, Z. Fan, General-purpose machine-learned potential for 16 elemental metals and their alloys, *Nature Communications* 15 (2024) 10208.
- [9] C. Zeni, R. Pinsler, D. Zügner, A. Fowler, M. Horton, X. Fu, Z. Wang, A. Shysheya, J. Crabbé, S. Ueda, R. Sordillo, L. Sun, J. Smith, B. Nguyen, H. Schulz, S. Lewis, C.-W. Huang, Z. Lu, Y. Zhou, H. Yang, H. Hao, J. Li, C. Yang, W. Li, R. Tomioka, T. Xie, A generative model for inorganic materials design, *Nature* (2025).
- [10] T. W. Ko, J. A. Finkler, S. Goedecker, J. Behler, Accurate fourth-generation machine learning potentials by electrostatic embedding, *Journal of Chemical Theory and Computation* 19 (2023) 3567–3579. PMID: 37289440.

- [11] A. P. Bartók, M. C. Payne, R. Kondor, G. Csányi, Gaussian approximation potentials: The accuracy of quantum mechanics, without the electrons, *Phys. Rev. Lett.* 104 (2010) 136403.
- [12] K. T. Schütt, P. Kessel, M. Gastegger, K. A. Nicoli, A. Tkatchenko, K.-R. Müller, Schnetpack: A deep learning toolbox for atomistic systems, *Journal of Chemical Theory and Computation* 15 (2019) 448–455.
- [13] J. Gasteiger, F. Becker, S. Günemann, Gemnet: Universal directional graph neural networks for molecules, in: *Conference on Neural Information Processing Systems (NeurIPS)*.
- [14] C. Ying, T. Cai, S. Luo, S. Zheng, G. Ke, D. He, Y. Shen, T.-Y. Liu, Do transformers really perform badly for graph representation?, in: *Thirty-Fifth Conference on Neural Information Processing Systems*.
- [15] G. L. W. Hart, T. Mueller, C. Toher, S. Curtarolo, Machine learning for alloys, *Nature Reviews Materials* 6 (2021) 730–755.
- [16] X. Liu, J. Zhang, Z. Pei, Machine learning for high-entropy alloys: Progress, challenges and opportunities, *Progress in Materials Science* 131 (2023) 101018.
- [17] Y.-W. Zhang, V. Sorkin, Z. H. Aitken, A. Politano, J. Behler, A. P Thompson, T. W. Ko, S. P. Ong, O. Chalykh, D. Korogod, E. Podryabinkin, A. Shapeev, J. Li, Y. Mishin, Z. Pei, X. Liu, J. Kim, Y. Park, S. Hwang, S. Han, K. Sheriff, Y. Cao, R. Freitas, Roadmap for the development of machine learning-based interatomic potentials, *Modelling and Simulation in Materials Science and Engineering* 33 (2025) 023301.
- [18] C. M. Clausen, J. Rossmeisl, Z. W. Ulissi, Adapting oc20-trained equiformerv2 models for high-entropy materials, *The Journal of Physical Chemistry C* 128 (2024) 11190–11195.
- [19] C. Chen, S. P. Ong, A universal graph deep learning interatomic potential for the periodic table, *Nature Computational Science* 2 (2022) 718–728.
- [20] B. Huang, G. F. von Rudorff, O. A. von Lilienfeld, The central role of density functional theory in the ai age, *Science* 381 (2023) 170–175.
- [21] C. Zeni, R. Pinsler, D. Zügner, A. Fowler, M. Horton, X. Fu, Z. Wang, A. Shysheya, J. Crabbé, S. Ueda, R. Sordillo, L. Sun, J. Smith, B. Nguyen, H. Schulz, S. Lewis, C.-W.

Huang, Z. Lu, Y. Zhou, H. Yang, H. Hao, J. Li, C. Yang, W. Li, R. Tomioka, T. Xie, A generative model for inorganic materials design, *Nature* (2025).

[22] W. Jia, H. Wang, M. Chen, D. Lu, L. Lin, R. Car, W. E, L. Zhang, Pushing the Limit of Molecular Dynamics with Ab Initio Accuracy to 100 Million Atoms with Machine Learning, IEEE Press.

[23] V. L. Deringer, N. Bernstein, G. Csányi, C. Ben Mahmoud, M. Ceriotti, M. Wilson, D. A. Drabold, S. R. Elliott, Origins of structural and electronic transitions in disordered silicon, *Nature* 589 (2021) 59–64.

[24] A. Musaelian, S. Batzner, A. Johansson, L. Sun, C. J. Owen, M. Kornbluth, B. Kozinsky, Learning local equivariant representations for large-scale atomistic dynamics, *Nature Communications* 14 (2023) 579.

[25] Z. Guo, D. Lu, Y. Yan, S. Hu, R. Liu, G. Tan, N. Sun, W. Jiang, L. Liu, Y. Chen, L. Zhang, M. Chen, H. Wang, W. Jia, Extending the limit of molecular dynamics with ab initio accuracy to 10 billion atoms, in: Proceedings of the 27th ACM SIGPLAN Symposium on Principles and Practice of Parallel Programming, PPoPP '22, Association for Computing Machinery, New York, NY, USA, 2022, p. 205–218.

[26] S. Doerr, M. Majewski, A. Pérez, A. Krämer, C. Clementi, F. Noe, T. Giorgino, G. De Fabritiis, Torchmd: A deep learning framework for molecular simulations, *Journal of Chemical Theory and Computation* 17 (2021) 2355–2363. PMID: 33729795.

[27] X. Gao, F. Ramezanghorbani, O. Isayev, J. S. Smith, A. E. Roitberg, Torchani: A free and open source pytorch-based deep learning implementation of the ani neural network potentials, *Journal of Chemical Information and Modeling* 60 (2020) 3408–3415. PMID: 32568524.

[28] T. Kostiuchenko, F. Körmann, J. Neugebauer, A. Shapeev, Impact of lattice relaxations on phase transitions in a high-entropy alloy studied by machine-learning potentials, *npj Computational Materials* 5 (2019) 55.

[29] Z. Wang, T. Yang, Chemical order/disorder phase transitions in nicofealtib multi-principal element alloys: A monte carlo analysis, *Acta Materialia* 285 (2025) 120635.

[30] J.-Z. Xie, X.-Y. Zhou, B. Jin, H. Jiang, Machine learning force field-aided cluster expansion approach to phase diagram of alloyed materials, *Journal of Chemical Theory and Computation* 20 (2024) 6207–6217. PMID: 38940547.

- [31] D. Jiang, L. Xie, L. Wang, Current application status of multi-scale simulation and machine learning in research on high-entropy alloys, *Journal of Materials Research and Technology* 26 (2023) 1341–1374.
- [32] F. Körmann, M. H. Sluiter, Interplay between lattice distortions, vibrations and phase stability in NbMoTaW high entropy alloys, *Entropy* 18 (2016).
- [33] X. Liu, J. Zhang, J. Yin, S. Bi, M. Eisenbach, Y. Wang, Monte carlo simulation of order-disorder transition in refractory high entropy alloys: A data-driven approach, *Computational Materials Science* 187 (2021) 110135.
- [34] J. Yin, Z. Pei, M. C. Gao, Neural network-based order parameter for phase transitions and its applications in high-entropy alloys, *Nature Computational Science* 1 (2021) 686–693.
- [35] T. Preis, P. Virnau, W. Paul, J. J. Schneider, Gpu accelerated monte carlo simulation of the 2d and 3d ising model, *Journal of Computational Physics* 228 (2009) 4468–4477.
- [36] J.-W. Yeh, S.-K. Chen, S.-J. Lin, J.-Y. Gan, T.-S. Chin, T.-T. Shun, C.-H. Tsau, S.-Y. Chang, Nanostructured high-entropy alloys with multiple principal elements: Novel alloy design concepts and outcomes, *Advanced Engineering Materials* 6 (2004) 299–303.
- [37] B. Cantor, I. Chang, P. Knight, A. Vincent, Microstructural development in equiatomic multicomponent alloys, *Materials Science and Engineering: A* 375-377 (2004) 213 – 218.
- [38] Z. Li, K. G. Pradeep, Y. Deng, D. Raabe, C. C. Tasan, Metastable high-entropy dual-phase alloys overcome the strength–ductility trade-off, *Nature* 534 (2016) 227.
- [39] T. Yang, Y. L. Zhao, Y. Tong, Z. B. Jiao, J. Wei, J. X. Cai, X. D. Han, D. Chen, A. Hu, J. J. Kai, K. Lu, Y. Liu, C. T. Liu, Multicomponent intermetallic nanoparticles and superb mechanical behaviors of complex alloys, *Science* 362 (2018) 933–937.
- [40] Y. Yang, T. Chen, L. Tan, J. D. Poplawsky, K. An, Y. Wang, G. D. Samolyuk, K. Littrell, A. R. Lupini, A. Borisevich, E. P. George, Bifunctional nanoprecipitates strengthen and ductilize a medium-entropy alloy, *Nature* 595 (2021) 245–249.
- [41] A. Ferrari, F. Körmann, M. Asta, J. Neugebauer, Simulating short-range order in compositionally complex materials, *Nature Computational Science* 3 (2023) 221–229.
- [42] J. Yin, Z. Pei, M. C. Gao, Neural network-based order parameter for phase transitions and its applications in high-entropy alloys, *Nature Computational Science* 1 (2021) 686–693.

[43] M. He, W. J. Davids, A. J. Breen, S. P. Ringer, Quantifying short-range order using atom probe tomography, *Nature Materials* 23 (2024) 1200–1207.

[44] B. Xiao, J. Luan, S. Zhao, L. Zhang, S. Chen, Y. Zhao, L. Xu, C. T. Liu, J.-J. Kai, T. Yang, Achieving thermally stable nanoparticles in chemically complex alloys via controllable sluggish lattice diffusion, *Nature Communications* 13 (2022) 4870.

[45] X. Han, G. Wu, S. Zhao, J. Guo, M. Yan, X. Hong, D. Wang, Nanoscale high-entropy alloy for electrocatalysis, *Matter* 6 (2023) 1717–1751.

[46] M. Li, F. Lin, S. Zhang, R. Zhao, L. Tao, L. Li, J. Li, L. Zeng, M. Luo, S. Guo, High-entropy alloy electrocatalysts go to (sub-)nanoscale, *Science Advances* 10 (2024) eadn2877.

[47] Y. Yao, Q. Dong, A. Brozena, J. Luo, J. Miao, M. Chi, C. Wang, I. G. Kevrekidis, Z. J. Ren, J. Greeley, G. Wang, A. Anapolsky, L. Hu, High-entropy nanoparticles: Synthesis-structure-property relationships and data-driven discovery, *Science* 376 (2022) eabn3103.

[48] J. Zhang, X. Liu, S. Bi, J. Yin, G. Zhang, M. Eisenbach, Robust data-driven approach for predicting the configurational energy of high entropy alloys, *Materials & Design* 185 (2020) 108247.

[49] J. Liu, P. Wang, J. Luan, J. Chen, P. Cai, J. Chen, X. Lu, Y. Fan, Z. Yu, K. Chou, Vase: A high-entropy alloy short-range order structural descriptor for machine learning, *Journal of Chemical Theory and Computation* 20 (2024) 11082–11092. PMID: 39046791.

[50] Y. Wang, G. M. Stocks, W. A. Shelton, D. M. C. Nicholson, Z. Szotek, W. M. Temmerman, Order-N multiple scattering approach to electronic structure calculations, *Phys. Rev. Lett.* 75 (1995) 2867–2870.

[51] M. Eisenbach, Y. W. Li, X. Liu, O. K. Odbadrakh, Z. Pei, G. M. Stocks, J. Yin, Lsms, 2017.

[52] X. Liu, Y. Wang, M. Eisenbach, G. M. Stocks, Fully-relativistic full-potential multiple scattering theory: A pathology-free scheme, *Computer Physics Communications* 224 (2018) 265–272.

[53] E. Prodan, W. Kohn, Nearsightedness of electronic matter, *Proceedings of the National Academy of Sciences* 102 (2005) 11635–11638.

- [54] Z. Fu, L. Jiang, J. L. Wardini, B. E. MacDonald, H. Wen, W. Xiong, D. Zhang, Y. Zhou, T. J. Rupert, W. Chen, E. J. Lavernia, A high-entropy alloy with hierarchical nanoprecipitates and ultrahigh strength, *Science Advances* 4 (2018).
- [55] Z. Li, K. G. Pradeep, Y. Deng, D. Raabe, C. C. Tasan, Metastable high-entropy dual-phase alloys overcome the strength–ductility trade-off, *Nature* 534 (2016) 227–230.
- [56] L. J. Santodonato, P. K. Liaw, R. R. Unocic, H. Bei, J. R. Morris, Predictive multiphase evolution in Al-containing high-entropy alloys, *Nature Communications* 9 (2018) 4520.
- [57] X.-G. Li, C. Chen, H. Zheng, Y. Zuo, S. P. Ong, Complex strengthening mechanisms in the NbMoTaW multi-principal element alloy, *npj Computational Materials* 6 (2020) 70.
- [58] S. Yin, Y. Zuo, A. Abu-Odeh, H. Zheng, X.-G. Li, J. Ding, S. P. Ong, M. Asta, R. O. Ritchie, Atomistic simulations of dislocation mobility in refractory high-entropy alloys and the effect of chemical short-range order, *Nature Communications* 12 (2021) 4873.
- [59] X. Wang, X. Meng, Z. Guo, M. Li, L. Liu, M. Li, Q. Xiao, T. Zhao, N. Sun, G. Tan, W. Jia, 29-billion atoms molecular dynamics simulation with ab initio accuracy on 35 million cores of new sunway supercomputer, *IEEE Transactions on Computers* (2025) 1–14.
- [60] X. Liu, J. Zhang, M. Eisenbach, Y. Wang, Machine learning modeling of high entropy alloy: the role of short-range order, *arXiv preprint arXiv:1906.02889* (2019).
- [61] S. Kirklin, J. E. Saal, B. Meredig, A. Thompson, J. W. Doak, M. Aykol, S. Rühl, C. Wolverton, The open quantum materials database (oqmd): assessing the accuracy of dft formation energies, *npj Computational Materials* 1 (2015) 15010.
- [62] W. P. Huhn, M. Widom, Prediction of A2 to B2 phase transition in the high-entropy alloy Mo-Nb-Ta-W, *JOM* 65 (2013) 1772–1779.
- [63] E. Zhang, Y. Tang, M. Wen, A. Obaied, I. Roslyakova, L. Zhang, On phase stability of mo-nb-ta-w refractory high entropy alloys, *International Journal of Refractory Metals and Hard Materials* 103 (2022) 105780.
- [64] Z. Fu, A. Hoffman, B. E. MacDonald, Z. Jiang, W. Chen, M. Arivu, H. Wen, E. J. Lavernia, Atom probe tomography study of an fe25ni25co25ti15al10 high-entropy alloy fabricated by powder metallurgy, *Acta Materialia* 179 (2019) 372–382.

[65] B. Block, P. Virnau, T. Preis, Multi-gpu accelerated multi-spin monte carlo simulations of the 2d ising model, *Computer Physics Communications* 181 (2010) 1549–1556.

[66] M. Lulli, M. Bernaschi, G. Parisi, Highly optimized simulations on single- and multi-gpu systems of the 3d ising spin glass model, *Computer Physics Communications* 196 (2015) 290–303.

[67] K. Yang, Y.-F. Chen, G. Roumpos, C. Colby, J. Anderson, High performance monte carlo simulation of ising model on tpu clusters, in: *Proceedings of the International Conference for High Performance Computing, Networking, Storage and Analysis, SC '19*, Association for Computing Machinery, New York, NY, USA, 2019.

[68] Y. Lin, F. Wang, X. Zheng, H. Gao, L. Zhang, Monte carlo simulation of the ising model on fpga, *Journal of Computational Physics* 237 (2013) 224–234.

[69] F. Ortega-Zamorano, M. A. Montemurro, S. A. Cannas, J. M. Jerez, L. Franco, Fpga hardware acceleration of monte carlo simulations for the ising model, *IEEE Trans. Parallel Distrib. Syst.* 27 (2016) 2618–2627.

[70] V. Yamakov, Parallel grand canonical monte carlo (paragrandmc) simulation code.

[71] K. Momma, F. Izumi, Vesta 3 for three-dimensional visualization of crystal, volumetric and morphology data, *Journal of Applied Crystallography* 44 (2011) 1272–1276.

[72] L. Onsager, Crystal statistics. i. a two-dimensional model with an order-disorder transition, *Phys. Rev.* 65 (1944) 117–149.

[73] R. H. Swendsen, J.-S. Wang, Nonuniversal critical dynamics in monte carlo simulations, *Phys. Rev. Lett.* 58 (1987) 86–88.

[74] F. Wang, D. P. Landau, Efficient, multiple-range random walk algorithm to calculate the density of states, *Phys. Rev. Lett.* 86 (2001) 2050–2053.

[75] U. Wolff, Collective monte carlo updating for spin systems, *Phys. Rev. Lett.* 62 (1989) 361–364.

[76] A. M. Ferrenberg, J. Xu, D. P. Landau, Pushing the limits of monte carlo simulations for the three-dimensional ising model, *Phys. Rev. E* 97 (2018) 043301.